

Insight into MoS₂–MoN Heterostructure to Accelerate Polysulfide Conversion toward High-Energy-Density Lithium–Sulfur Batteries

Sizhe Wang, Shaopei Feng, Jianwen Liang, Qingmei Su, Feipeng Zhao, Haojie Song,*
Matthew Zheng, Qian Sun, Zhongxin Song, Xiaohua Jia, Jin Yang, Yong Li, Jiaxuan Liao,
Ruying Li, and Xueliang Sun*

Lithium–sulfur batteries are deemed as optimal energy devices for the next generation of high-energy-density energy storage. However, several problems such as low energy density and short cycle life hinder their application in industry. Here, MoS₂–MoN heterostructure nanosheets grown on carbon nanotube arrays as free-standing cathodes are reported. In this heterostructure, MoN works as a promoter to provide coupled electrons to accelerate the redox reaction of polysulfides while the MoS₂, with a two-dimensional layered structure, provides smooth Li⁺ diffusion pathways. Through their respective advantages, both MoN and MoS₂ could mutually boost the process of “adsorption-diffusion-conversion” of polysulfides, which have a synergy enhancement effect to restrain the lithium polysulfides from shuttling. The designed cathodes show excellent long-term cycling performances of 1000 cycles at 1C with a low decay rate of 0.039% per cycle and a high rate capability up to 6C. A high initial areal capacity of 13.3 mAh cm⁻² is also achieved under a low electrolyte volume/sulfur loading (E/S) ratio of 6.3 mL g⁻¹. This strategy of promoting polysulfide conversion by heterostructure MoS₂–MoN as presented in this work can provide a more structured design strategy for future advanced Li–S energy storage systems.

1. Introduction

To fulfill the ever-increasing green energy demand, pushed forward by current-day and future consumer electronics, the lithium–sulfur (Li–S) battery is becoming an increasingly attractive solution. The Li–S battery has a high intrinsic energy density of about 2600 kW kg⁻¹ and sulfur is a low-cost and abundant resource that is environmentally friendly and safe.^[1] However, facing rigorous practical application standards, Li–S batteries are hindered by the challenges of low energy density and poor cycle life in application due to the sluggish redox kinetics of S₈ ↔ Li₂S caused by lithium polysulfides (LiPSs) shuttling and poor conductivity of S₈.^[2]

Numerous strategies have been provided to address these problems, such as designing sulfur hosts, adding functional interlayers, modifying the surface of separators, protecting lithium anodes and so on.^[3] Among them, most of the efforts focus on the design and construction of sulfur hosts.^[4] Other than the carbon-based materials used to hold the active sulfur, a large amount of different inorganic/organic compounds added were functional additives used to regulate and/or catalyze the LiPSs, aiming to erase the negative impacts of the shuttling effect.^[5] Different additives have different functionalities on polysulfides, such as van der Waals interactions to absorb polar LiPS species,^[2] low diffusion barriers to facilitate surface migration of LiPSs,^[6] or the ability to catalyze and transform long-chain LiPSs into insoluble Li₂S.^[5b,7] However, single additives always achieve a single side of functionality. A clear example is that a polar semiconductor will impede the direct surface conversion of LiPSs on the polar host due to low conductivity.^[8] Thus, combining two compounds to integrate multiple respective functionalities together is a novel way to alleviate the polysulfide shuttling issue.^[9] Yang and coworkers constructed a twinborn TiO₂–TiN heterostructure that combined the merits of highly adsorptive TiO₂ with conducting TiN and achieved smooth trapping-diffusion-conversion of LiPSs.^[10] Afterward, Liu and coworkers prepared a binary VO₂–VN host to combine the merits of

Dr. S. Z. Wang, S. P. Feng, Prof. Q. M. Su, Prof. H. J. Song, Prof. X. H. Jia, Dr. J. Yang, Dr. Y. Li

School of Materials Science and Engineering
Shaanxi Key Laboratory of Green Preparation and Functionalization
for Inorganic Materials
Shaanxi University of Science & Technology
Xi'an 710021, P. R. China
E-mail: songhaojie@sust.edu.cn

Dr. S. Z. Wang, Dr. J. W. Liang, F. P. Zhao, M. Zheng, Dr. Q. Sun,
Dr. Z. X. Song, R. Y. Li, Prof. X. L. Sun
Department of Mechanical and Materials Engineering
University of Western Ontario
London, Ontario N6A 5B9, Canada
E-mail: xsun9@uwo.ca

Dr. S. Z. Wang, Prof. J. X. Liao
School of Materials and Energy
University of Electronic Science and Technology of China
Chengdu 611731, P. R. China

 The ORCID identification number(s) for the author(s) of this article can be found under <https://doi.org/10.1002/aenm.202003314>.

DOI: 10.1002/aenm.202003314

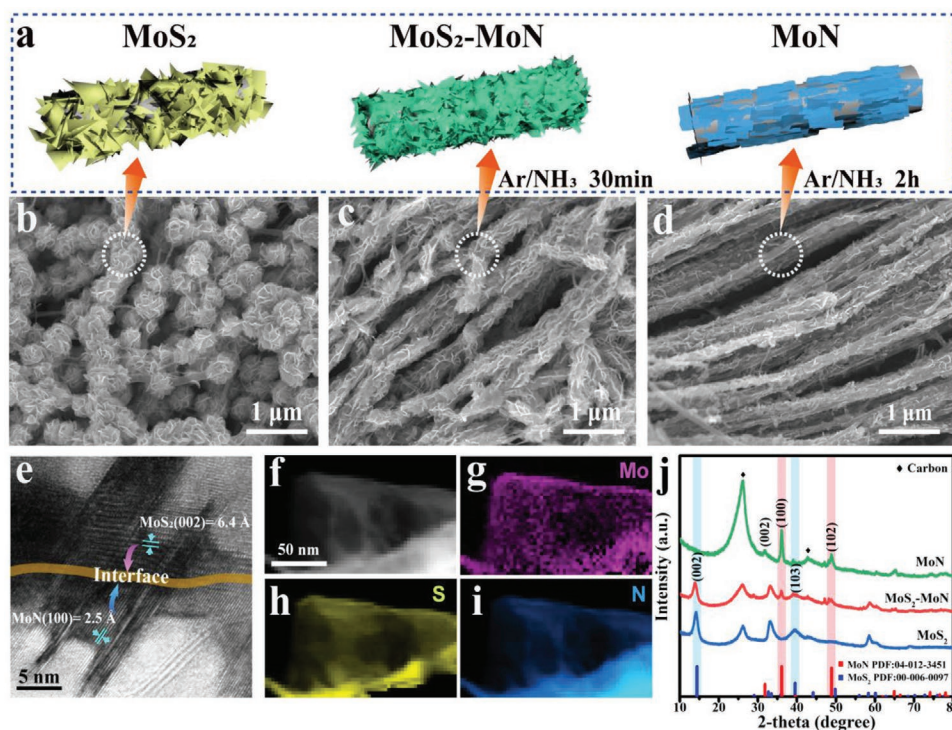


Figure 1. a) Schematic illustration of MoS₂, MoS₂-MoN, and MoN nanosheets grown on NCNT vertically; SEM images of b) MoS₂, c) MoS₂-MoN, and d) MoN hosts; e) HRTEM images of interface between MoS₂ and MoN in MoS₂-MoN host; f-i) STEM images and corresponding EELS mapping images of MoS₂-MoN host; j) XRD patterns of MoS₂, MoS₂-MoN, and MoN hosts.

ultrafast anchoring (VO₂) with electronic conducting (VN) to accomplish immobilization-diffusion-conversion of LiPSs.^[11]

MoS₂, a typical two-dimension layered disulfide, has been applied to work as an additive in sulfur hosts due to its moderate polar reaction with LiPSs and fast Li ion surface diffusion.^[12] Nevertheless, the low intrinsic electron conductivity of MoS₂ will restrict the redox kinetics of S₈ ↔ Li₂S greatly. To remedy the weak conductivity of MoS₂, MoN seemed like an ideal candidate. MoN is a selective metallic compound with molybdenum cation that will accelerate redox kinetics due to its high intrinsic electron conductivity ($4.55 \times 10^6 \text{ S m}^{-1}$).^[13] Furthermore, the optimizations of bonding orbital hybridization or interface defect/strain evolution would cause a stronger interaction of Mo atoms toward adsorbed polysulfide.^[14] Based on these considerations, MoS₂-MoN heterostructure nanosheets were grown vertically on nitrogen-doped carbon nanotube (NCNT) arrays, which were designed to work as sulfur hosts. As a result, moderate LiPS trapping and fast surface Li⁺ diffusion (by MoS₂), combined with intrinsically high conductivity and coupled electron transfer through the redox reaction (by MoN) for LiPS conversion can be simultaneously realized on the heterostructure surface, enabling synergistic trapping-diffusion-catalytic conversion of LiPSs. The MoS₂-MoN/S cathode achieved excellent electrochemical performances, demonstrating a stable long-term cycling ability with a low decay rate of 0.039% per cycling up to 1000 cycles at 1C and high rate capability up to 6C. To achieve high gravimetric energy density at a commercial level, the cathode assembled with a low E/S ratio of 6.3 mL g⁻¹ were tested. A high initial areal capacity of 13.3 mAh cm⁻² is achieved, which further certifies the advantage of the designed cathodes.

2. Results and Discussion

The schematic illustration of MoS₂, MoS₂-MoN, and MoN host morphologies is illustrated in **Figure 1a**. The MoS₂ nanoflowers were grown on the surface of NCNT array uniformly by a hydrothermal process, as shown in scanning electron microscopic (SEM) images in **Figure 1b**. The transmission electron microscopy (TEM) micrographs of flower shaped MoS₂ wrapped the bamboo-like NCNTs with sectional joints (**Figure S1**, Supporting Information). To synergize the functions of MoS₂ and MoN, we used in situ gas nitridation technology to treat the MoS₂ host under NH₃ for 30 min. After this treatment, parts of the MoS₂ nanoflowers transformed into MoN nanosheets to form the heterostructure MoS₂-MoN binary host. The pure MoN hosts were also prepared for comparison by treating under NH₃ for 2 h. As shown in **Figure 1c**, the shape of MoN nanosheets transform from vertical to horizontal on the surface of NCNT after the nitridation. The Brunauer-Emmett-Teller (BET) surface area of MoN host decreases after the nitrogenization process accordingly (**Figure S3**, Supporting Information). HRTEM images with clear lattice fringes were used to investigate the crystalline structure of MoS₂-MoN binary host (**Figure 1e**). It could easily identify that the (002) plane with d-spacing ≈ 0.64 nm from MoS₂^[15] and (100) plane with d-spacing ≈ 0.25 nm from MoN^[16] co-existed in the same nanosheet. The HRTEM images of the pure MoS₂ and MoN hosts were also shown in **Figure S2** in the Supporting Information. The electron energy loss spectroscopy (EELS) mapping images (**Figure 2h-m**) of Mo (purple), S (yellow), and N (blue) elements also confirmed the co-exist of MoS₂ and MoN binary

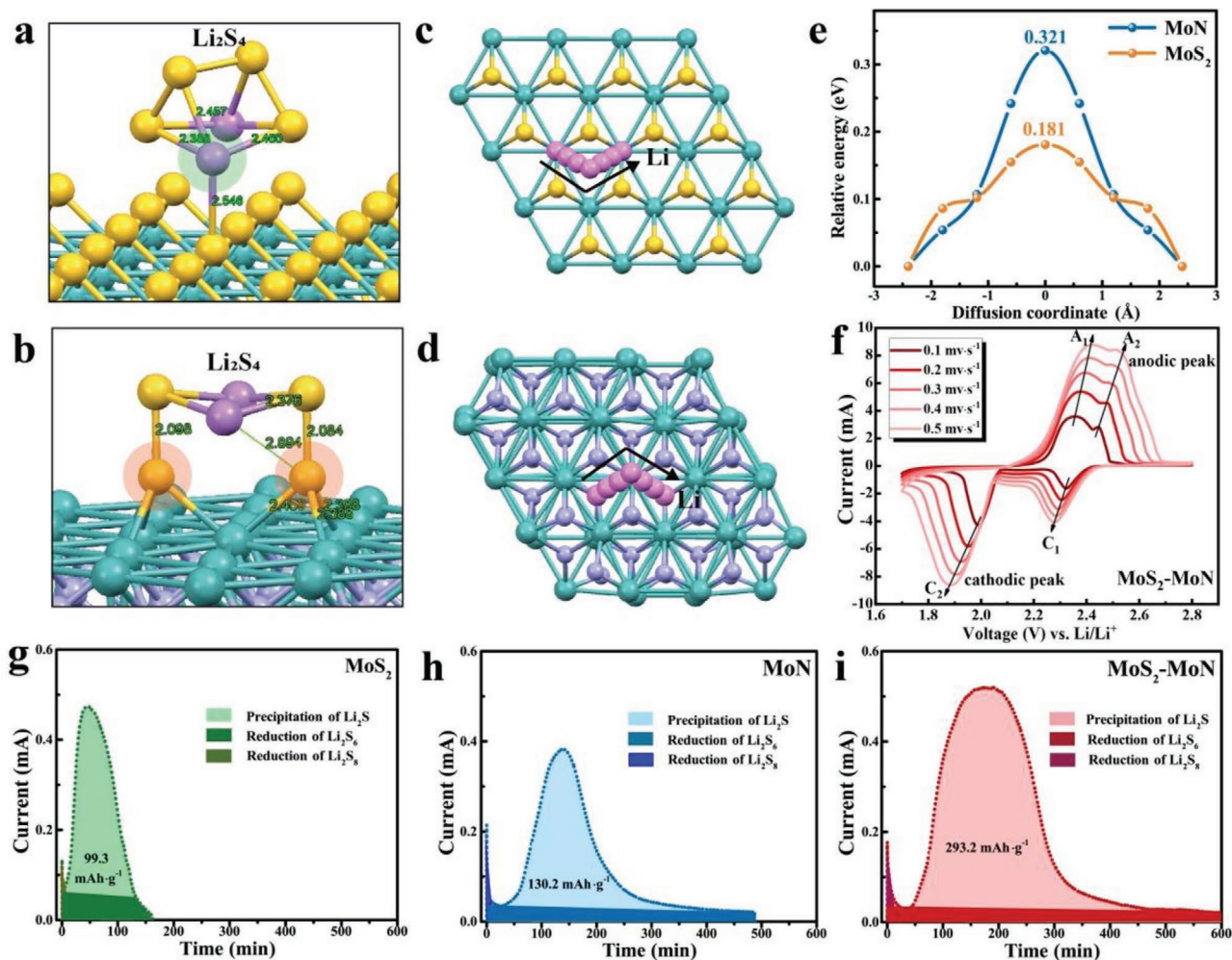


Figure 2. The molecular structures of Li_2S_4 adsorptions on a) MoS_2 (100) and b) MoN (100); The molecular structures of Li ion diffusion pathways on c) MoS_2 host and d) MoN host; e) the corresponding Li ion diffusion barriers profiles. f) The CV curves of MoS_2 - MoN cathodes with various scanning rate from 0.1 to 0.5 mV s^{-1} . Potentiostatic discharge curves of a Li_2S_8 solution at 2.05 V on the surfaces of g) MoS_2 , h) MoS_2 - MoN , and i) MoN hosts.

nanosheets uniformly. The elemental mapping images at a low magnification agreed with the uniform MoS_2 - MoN elemental distribution at a larger scale (Figure S4, Supporting Information). The X-ray diffraction (XRD) patterns of these three hosts were shown in Figure 1j. All the main diffraction peaks of MoS_2 host agree well with the hexagonal phase of MoS_2 with a space group of $\text{P63}/\text{mmc}$ (JCPDS 00-006-0097). Likewise, the MoN host shows the hexagonal phase with a space group of $\text{P63}/\text{mmc}$ (JCPDS 04-012-3451), where there is none of the second phase from MoS_2 . The MoS_2 - MoN binary host shows an intermediate state of co-existing of MoS_2 and MoN phases, which matches the unique heterostructure of MoS_2 - MoN binary host. In Figure S5 in the Supporting Information, the intensive Raman peaks at 379.9 and 406.5 cm^{-1} were correspondent to the typical E_{2g}^1 and A_{1g} mode of 2H MoS_2 .^[17] The Raman spectra of MoN and MoS_2 - MoN are similar to the vibration's mode of MoS_2 . A new peak at 482.7 cm^{-1} may be derived from Mo-N vibrations mode.

Three kinds of typical LiPSs solutions (Li_2S_4 , Li_2S_6 , and Li_2S_8) were used to visualize the interactions between the

heterostructure host and LiPSs (Figure S6, Supporting Information). The MoS_2 , MoS_2 - MoN , and MoN hosts were separately mixed with the LiPSs solution, which was yellowish in color. To exclude the functionality of NCNT substrate, the NCNT paper was also tested. For all these absorption tests, the NCNT paper exhibited hardly any color change of solutions, indicating negligible adsorption effects on LiPSs. The MoS_2 and MoN hosts show weak absorbing ability to LiPSs, accounted by the fade in color of solutions. It is noteworthy that the MoS_2 and MoN hosts show different adsorption effects to Li_2S_4 , Li_2S_6 , and Li_2S_8 solutions. After MoS_2 - MoN host is added in these three LiPS-containing solutions, the yellowish color turns clear and colorless, in sharp contrast to the other tests. Through these visualized absorption tests, it is suggested that this heterostructure host has much stronger affinities capabilities on long-chain LiPSs than the single MoN or MoS_2 host.

Density functional theory (DFT) calculations were used to uncover the interactions between MoS_2 (MoN) and long-chain LiPSs. The molecular structure models of MoS_2 (100) interacting with LiPS (Li_2S_n , $n = 4, 6, 8$) geometries are

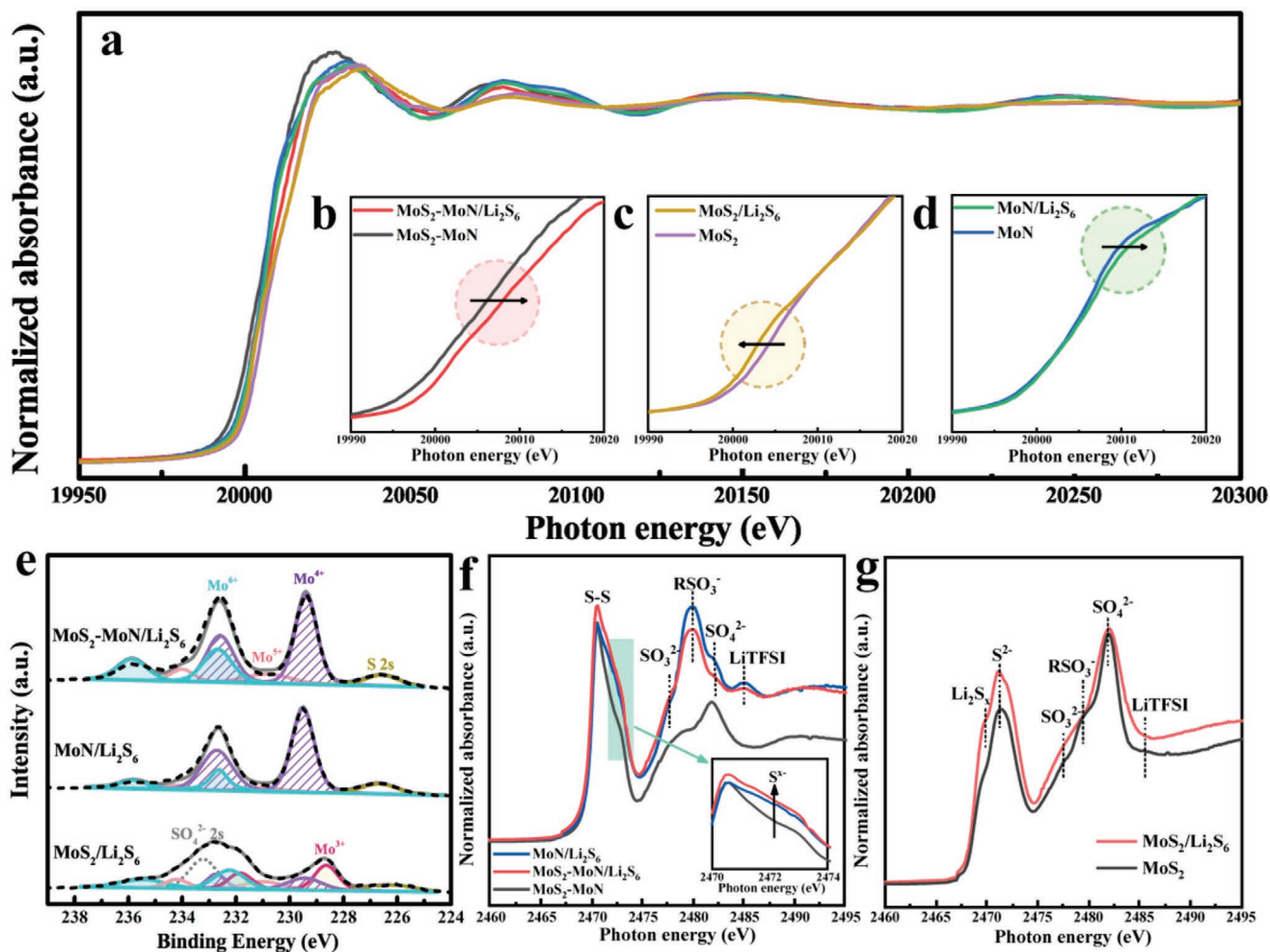


Figure 3. a–d) HXMA spectra of molybdenum K-edge (Enlarged part of the pre-edge for b) MoS₂–MoN, c) MoS₂, and d) MoN hosts) before/after soaking in Li₂S₆ solutions; e) XPS spectra of Mo 3d peaks for MoS₂, MoN, and MoS₂–MoN hosts after soaking in Li₂S₆ solution; f, g) SXRMB spectra of sulfur K-edge for MoS₂–MoN, MoS₂, and MoN hosts before/after soaking in Li₂S₆ solutions.

shown in Figure 3a and Figure S7 (Supporting Information). The corresponding absorption energies is calculated to be -0.44 , -0.271 , and -0.323 eV, respectively. For MoN (100), it is worth noting that the Li–S bonds in Li₂S₄ are broken due to the strong interaction between Li₂S₄ and MoN (100) surface, resulting in partial sulfurization of the surface dangling bond of Mo in MoN (100) (Figure 3b; Figure S8, Supporting Information). A similar phenomenon has been reported in Li₂S₆ on Co₄N.^[18] The generalized synchronous transit (LST/QST) is applied for computing Li⁺ transition state. The diffusion energy barrier is the energy difference between the total energies of transition state and the initial defective structure. The calculation of Li ion diffusion pathways on the surface of MoS₂ and MoN were performed and shown in Figure 2c,d. Typically, Li ion diffusion process is a limited kinetics process due to the low electron and Li ion conductivity of S and resulted polysulfide products. Thus, a fast lithium ion diffusion in substrate could facilitates the sulfur transformation chemistry. According to the Li ion diffusion barrier profiles calculated by climbing image nudged elastic band in Figure 2e, the MoS₂ showed lower barrier with peak

value of 0.181 eV, while the peak value of MoN is 0.321 eV, thus reflecting MoS₂'s better Li ion diffusion capability and stronger interfacial ions transfer dynamics in MoS₂ substrate. Furthermore, cyclic voltammetry (CV) testing at 0.1–0.5 mV s⁻¹ rates were used to evaluate the lithium ion diffusion coefficient (Figure 2f; Figure S9, Supporting Information, details are in Supporting Information). The corresponding fitted lines of ln (peak current) versus ln (scan rate) plots at cathodic/anodic peaks (named as A₁, A₂, C₁, C₂) are shown in Figure S10 in the Supporting Information. The slopes of the MoN hosts show the lowest values, suggesting the weakest lithium ion diffusion capability among these three hosts.^[19] It is a remarkable fact that the C1 peaks (at around 2.0 V) of the pure MoS₂ host disappeared due to the high polarization and weak redox kinetics of the transformations from the LiPSs to insoluble Li₂S. In stark contrast, the MoS₂–MoN hosts show obvious enhancement of the slope values within the MoS₂ part, indicating that the MoS₂ and MoN have a synergistic enhancement effect that helps achieve the best kinetics performances, rather than a sum of independent influences from MoS₂ (or MoN).

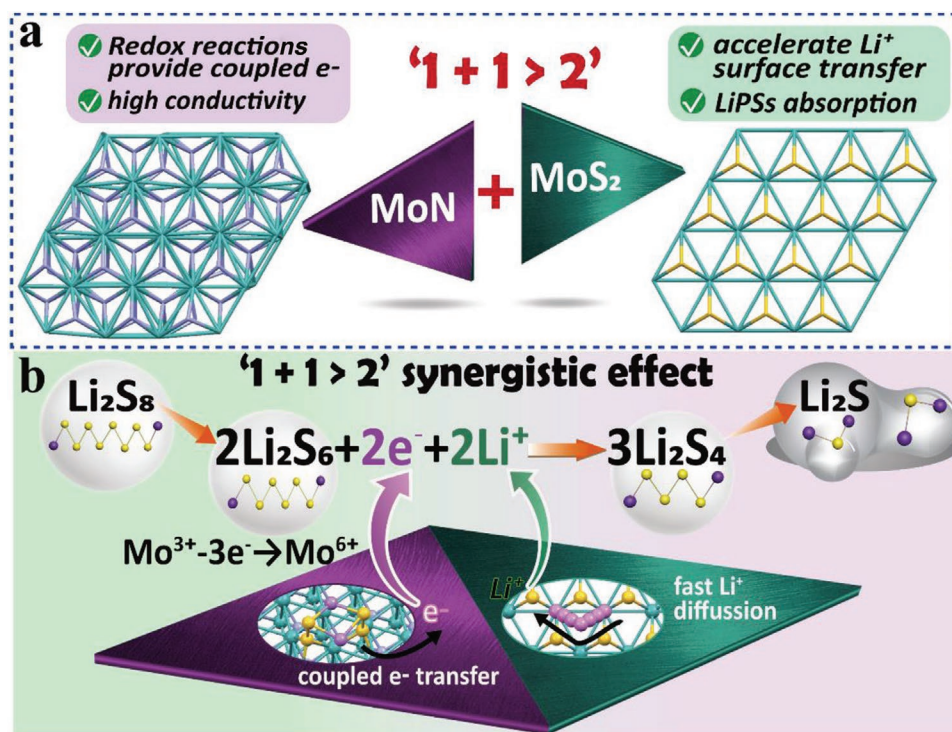


Figure 4. a) Structural features of each part of heterostructure MoS_2 - MoN host. b) Schematic illustration of synergistic catalytic conversion of LiPSs by the MoS_2 - MoN host during the charge/discharge processes.

To demonstrate the superiority of MoS_2 - MoN host with respect to the Li_2S precipitation conversion process, potentiostatic discharge curves of MoS_2 , MoS_2 - MoN , and MoN cells were tested at 2.05 V by using Li_2S_8 solution as electrolyte (Figure 2h-j). The capacities of MoS_2 host and MoN host derived from Li_2S precipitation are ≈ 99.3 and ≈ 130.2 mAh g^{-1} , separately. In contrast, the capacity of VS@NT host was almost 2–3 times larger (≈ 293.2 mAh g^{-1}) based on Faraday's law.^[20] To further identify the LiPSs conversion promoted by MoS_2 - MoN , the CV analyses of symmetrical cells with Li_2S_6 solution as electrolyte were tested in Figure S11a in the Supporting Information. Compared with the MoS_2 and MoN cells, the current polarization curve of the MoS_2 - MoN cell shows a much larger area, demonstrating that MoS_2 - MoN not only demonstrates the better electrochemically trapping capability but also the stronger catalytic conversions of LiPSs. The lower impedances of MoS_2 - MoN cell (Figure S11b, Supporting Information) also demonstrated that effective synergetic catalytic conversion of LiPS by MoS_2 - MoN host.

To identify the detailed reaction mechanisms between the LiPSs and MoS_2 - MoN host, X-ray absorption near edge structure (XANES) spectra of Mo L-edge, S K-edge, Mo K-edge were tested through the Soft X-ray Micro-characterization Beamline (SXRMB) and Hard X-ray Micro-Analysis (HXMA), separately (Figure 3; Figure S12, Supporting Information). To avoid interference derived from functional groups and charge/discharge products in the electrolyte, we used Li_2S_6 , a probe species that represents a polysulfide at an average depth of discharge, to investigate the reaction products. In Figure 3a, all these curves of Mo K-edge show similar peak shape due to the similar

elementary composition. However, it is easy to find clear differences among these samples after enlarging the pre-edge of these curves. The Mo pre-edge in MoS_2 host moves to a lower energy position slightly (Figure 3c). On the contrary, the Mo pre-edges in MoS_2 - MoN and MoN hosts shift to higher energy positions (Figure 3b,d), indicating that the valance of Mo ions ascend after reaction with Li_2S_6 .^[21] Except for the Mo^{4+} derived from the pristine MoS_2 , distinct Mo^{6+} 3d peaks appeared at 232.7 and 235.8 eV (Figure 3e), also demonstrating the redox reaction between MoN and Li_2S_6 . Through the oxidation of MoN ($\text{Mo}^{3+} - 3e^- \rightarrow \text{Mo}^{6+}$), the coupled electrons transfer from Mo^{3+} to S_x^{2-} in LiPSs.^[22] For the S K-edge in Figure 3f, the peaks at 2477.6, 2480, and 2482.2 eV are attributed to SO_3^{2-} , RSO_3^- , and SO_3^{2-} , respectively,^[23] corresponding to the X-ray photoelectron spectroscopy (XPS) spectrum of S 2p peaks at around 169 eV (Figure S13, Supporting Information). In Figure 3g, the intensities of peaks around 2472 eV in MoS_2 - $\text{MoN}/\text{Li}_2\text{S}_6$ and $\text{MoN}/\text{Li}_2\text{S}_6$ samples increase after soaking in Li_2S_6 solution. According to the former DFT calculation results, the peaks may represent the bonds of S-Mo, which is derived from the interaction between Li_2S_6 and MoN .

After the analysis of LiPSs reaction mechanism with the MoS_2 - MoN host, we can conclude the structural features of each part of this heterostructure host (Figure 4a). On one hand for MoN part, this part could provide the coupled electron to accelerate the conversion from Li_2S_x ($x > 2$) to Li_2S through the oxidation reaction with LiPSs. Meanwhile, the intrinsic high electron conductivity does well in enhancing the redox kinetics. On the other hand for MoS_2 part, moderate absorption capability helps to regulate LiPSs around the cathode.

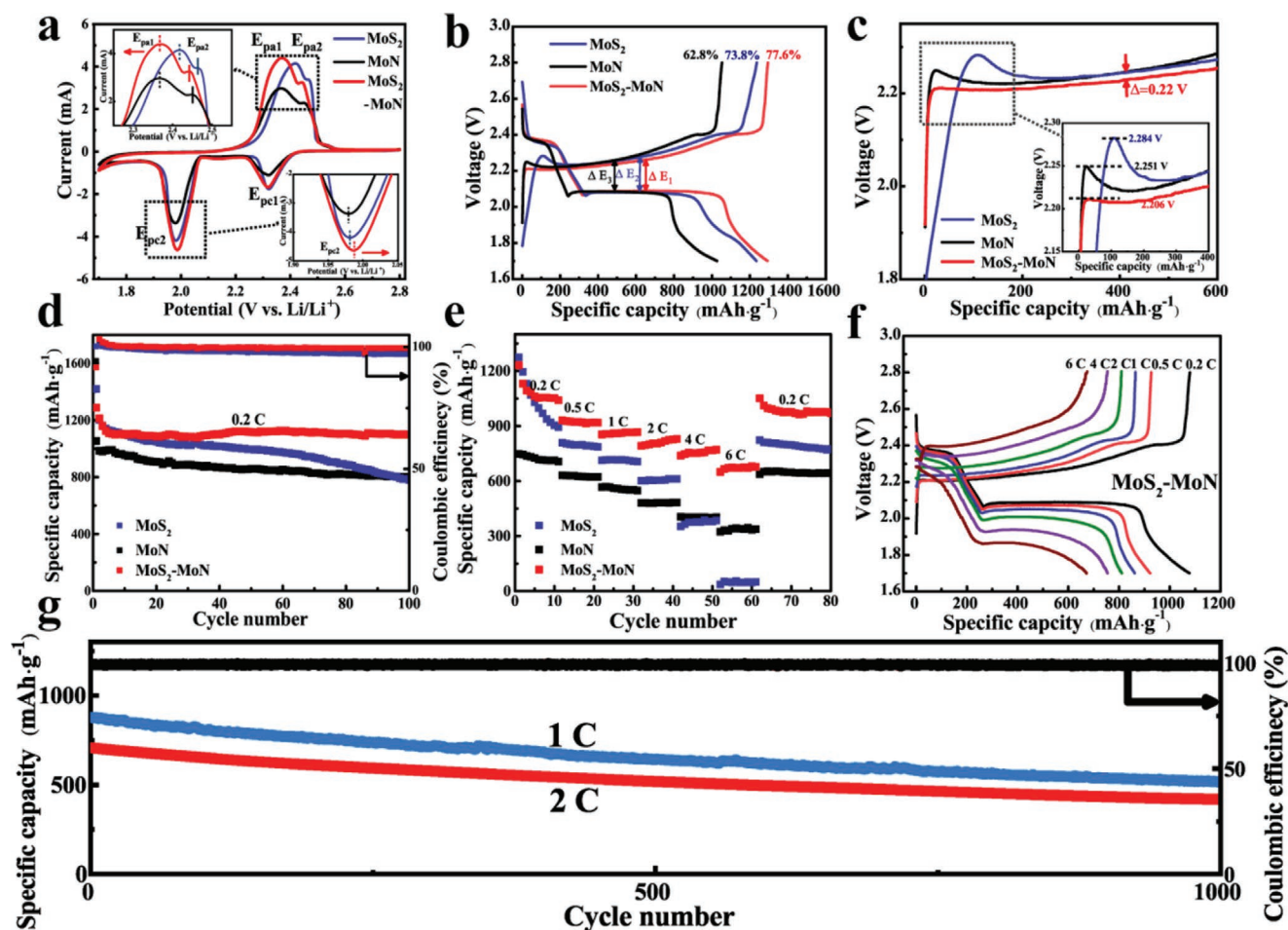


Figure 5. a) CV curves at a scanning rate of 0.2 mV s^{-1} ; b) the galvanostatic charge/discharge curves; c) the enlarged part for charge voltage profiles of the first cycle; d) cyclic performances at 0.2 C for 100 cycles; e) rate performance at various current densities from 0.2 C to 6 C of MoS_2/S , MoN/S , and $\text{MoS}_2\text{-MoN}/\text{S}$ cathodes. f) The galvanostatic charge/discharge curve at different current rates of $\text{MoS}_2\text{-MoN}/\text{S}$ cathode. g) Long-term cycling performance at 1 C and 2 C of $\text{MoS}_2\text{-MoN}/\text{S}$ cathode for 1000 cycles.

Furthermore, the intrinsic layer structure of MoS_2 provides fast Li^+ diffusion paths with low diffusion energy barriers. Schematic illustration of synergistic catalytic conversion of LiPS by $\text{MoS}_2\text{-MoN}$ host in a Li-S battery model is summarized in Figure 4b. Based on the former experimental and theoretical calculation results, we can conclude the existence of a synergistic catalytic conversion mechanism. Taking the transformation process (Li_2S_6 to Li_2S_4 , $2\text{Li}_2\text{S}_6 + 2\text{Li}^+ + 2\text{e}^- \rightarrow 3\text{Li}_2\text{S}_4$) as an instance, MoN nanosheets will react with Li_2S_6 to provide the coupled e^- and MoS_2 nanosheets with fast Li^+ diffusion paths to provide the Li^+ to participate in the transfer reaction. The use of both MoN and MoS_2 results in a synergistic performance that exceeds the individual benefits that they provide (defined as “ $1 + 1 > 2$ ”). Through the synergistic effect of MoS_2 and MoN, the $\text{MoS}_2\text{-MoN}$ host will accelerate the chemical reaction from Li_2S_6 to Li_2S_4 ($2\text{Li}_2\text{S}_6 + 3\text{Li}^+ + \text{Mo}^{3+} \rightarrow 3\text{Li}_2\text{S}_4 + \text{Mo}^{6+}$) considerably, enabling “ $1 + 1 > 2$ ” synergistic effect of trapping-diffusion-catalytic conversion of LiPSs efficiently.

Standard CR2032-type coin cells with MoS_2/S , $\text{MoS}_2\text{-MoN}/\text{S}$, and MoN/S as the cathode were assembled to measure the elec-

trochemical performances. Figure 5a displays the CV curves of the MoS_2/S , $\text{MoS}_2\text{-MoN}/\text{S}$, and MoN/S cathodes at a scan rate of 0.1 mV s^{-1} . The peak shapes of $\text{MoS}_2\text{-MoN}/\text{S}$ cell were stronger than those of the MoS_2/S and MoN/S cell, indicating faster kinetics of the $\text{MoS}_2\text{-MoN}/\text{S}$ cell for Li-ion diffusion across the cathode material. Compared with the MoS_2/S cell, the anodic peaks of $\text{MoS}_2\text{-MoN}/\text{S}$ cell shift to lower potentials in the charge sweep and the cathodic peaks of $\text{MoS}_2\text{-MoN}/\text{S}$ cell shift to higher potentials in the discharge sweep, indicating that the $\text{MoS}_2\text{-MoN}/\text{S}$ cell facilitates faster sulfur redox reactions and significantly faster kinetics during cycling.^[5b] The voltage plateaus of galvanostatic charge/discharge profiles (Figure 5b) are also correspondent to the peaks in the CV curves. Compared with the initial charge capacity of MoS_2/S ($1234.7 \text{ mAh g}^{-1}$) and MoN/S ($1026.9 \text{ mAh g}^{-1}$) cells, the charge/discharge plateaus of $\text{MoS}_2\text{-MoN}/\text{S}$ were much longer, leading to a larger capacity of $1292.9 \text{ mAh g}^{-1}$ and enhanced sulfur utilization of 77.6%. Additionally, $\text{MoS}_2\text{-MoN}/\text{S}$ deliver the lowest plateaus of oxidation voltage and the smallest voltage gap between oxidation and reduction plateaus.^[24] When these cells operate under almost quasi-equilibrium conditions, the galvanostatic intermittent

titration technique (GITT) curves of MoS₂-MoN/S with the lower charging voltage plateaus and smaller variations of quasi-open-circuit-voltages (Figure S14, Supporting Information) again confirm that the electrochemical kinetics are accelerated by heterostructural MoS₂-MoN intensively.^[25]

To further evaluate the catalytic ability of these three cathode materials, the initial activation energy barrier of Li₂S on various electrode materials was investigated (Figure 5c). The MoS₂/S cathode showed a clear voltage jump with the highest potential barrier of 2.28 V during initial charging process due to the semiconducting character of MoS₂ with low electron conductivity. Notably, the MoS₂-MoN/S cathode delivered the lowest potential barrier at about 2.206 V without obvious voltage jump peak, indicating an accelerated activation process with low charge transfer resistance.^[19] The charge voltage plateaus after the short voltage jump represent the phase conversion reaction from Li₂S to low-order LiPSs.^[7] The voltage gap between MoS₂-MoN/S cathode and MoS₂/S (or MoN/S) is more than 0.22 V, further proving that the lower polarization of the charging process with the accelerated electrochemical kinetics was driven by MoS₂-MoN. The impedance of the MoS₂-MoN/S cell after cycling was also consistently smaller than that of the MoS₂/S and MoN/S cells (Figure S15, Supporting Information).

In Figure 5d, short cycling performance at a current density of 0.2C of these three cathodes were tested (1C = 1672 mA g⁻¹). The MoS₂-MoN/S cathode delivered the highest capacity and best cycling stability among the sulfur electrodes with a high reversible discharge capacity of ≈1100 mAh g⁻¹ and capacity retention of 93.9% after 100 cycles (compared to the 2nd cycle). In comparison, the MoN/S cathode delivered a gradual fading

process with capacity retention of 81.4% after 100 cycles. More obviously, the capacity of the MoS₂/S cathode faded rapidly with a capacity retention of only 64.9% after 100 cycles. The rate capabilities were measured under a current density range from 0.2C to 6C (Figure 5d). The histograms of capacities versus scan rates for these three hosts are summarized in Figure S16 in the Supporting Information. The corresponding galvanostatic charge/discharge profiles were shown in Figure 5f and Figure S17 (Supporting Information). The average reversible capacities of the MoS₂-MoN/S cathode are 1078, 924, 865, 815, 761, and 674 mAh g⁻¹ at rates of 0.2C, 0.5C, 1C, 2C, 4C, and 6C, respectively. Even when the current density was up to 6C, it was still easy to identify a distinct two-plateau charge-discharge profile, further confirming the MoS₂-MoN host achieves fast sulfur redox reaction kinetics. The MoN/S cathode showed a similar rate stability but much lower capacity and sulfur utilization. In contrast, the MoS₂/S cathode showed poor rate capacity of only 54 mAh g⁻¹ when testing at the 6C rate and failed to maintain the 2nd discharge plateau at 4C.

To further testify to the long-term cycling stability of the MoS₂-MoN/S cathode, the cycling performance at 1C and 2C for 1000 cycles is shown in Figure 5g. The cell maintained stable cycling performance with a low capacity decay rate of 0.039%/0.041% per cycle at 1C/2C rates. Even after 1000 cycles, the electrode still delivered high reversible capacities of 520/459 mAh g⁻¹. Another visual observation in terms of disassembled cathodes after 1000 cycles verified that the MoS₂-MoN/S host after long-term cycling still maintain the original morphology, suggesting high structural stability of the MoS₂-MoN host (Figure S18, Supporting Information). Comparisons with recent works on

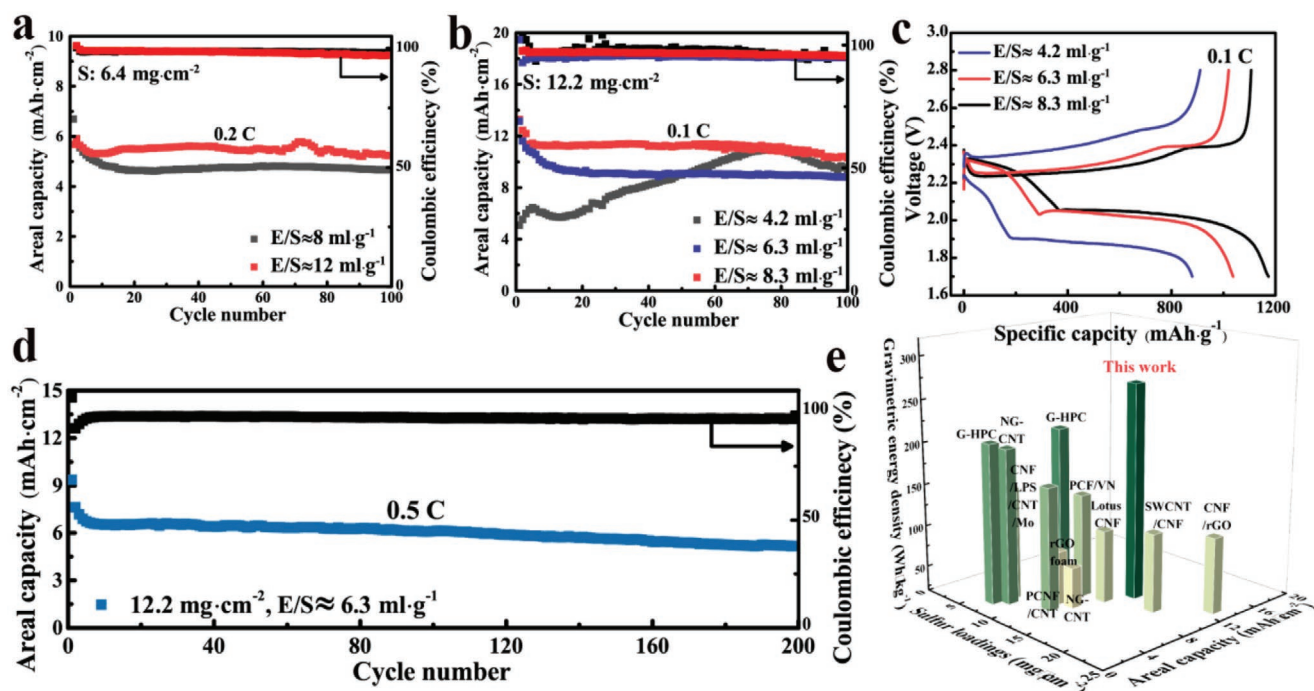


Figure 6. Cycling performances of MoS₂-MoN/S cathodes with sulfur loadings of a) 6.4 mg cm⁻² with different E/S ratios at 0.2C and b) 12.2 mg cm⁻² with different E/S ratios at 0.1C for 100 cycles. c) Galvanostatic charge/discharge curves for different E/S ratios with sulfur loadings of 12.2 mg cm⁻². d) Cycling performance of MoS₂-MoN/S cathode with 12.2 mg cm⁻² S loadings and 6.3 ml g⁻¹ E/S ratio at 0.5C for 200 cycles. e) Performance comparisons with recent works on free-standing high sulfur loading Li-S batteries cathodes.

Mo-based materials for application in Li–S batteries are shown in Table S1 in the Supporting Information. Comparisons with recent works on heterostructure materials for application in Li–S batteries are shown in Table S2 in the Supporting Information. The leading results further support the superiority of heterostructure MoS₂–MoN host for high capacity with stable long-term cycling.

To satisfy the commercial standards for application in next-generation energy storage devices, the sulfur loading and the electrolyte volume have been regarded as two critical factors for the practical applications of Li–S batteries at an industrial level.^[26] Thus, the cycling and rate performances of MoS₂–MoN/S cathodes with low usage of electrolytes (E/S < 12 mL g⁻¹) and high sulfur loadings (6.4 and 12.2 mg cm⁻²) were investigated. The sulfur content (in S/C composite) is measured through the TG curves under Ar₂ (Figure S19, Supporting Information, details are in Supporting Information). In Figure 6a, the MoS₂–MoN/S cathode with a sulfur loading of 6.4 mg cm⁻² and E/S = 12 mL g⁻¹ shows an initial areal capacity of 6.0 mAh cm⁻² at 0.2C and high capacity retention of 87.8% after 100 cycles. When the E/S ratio is decreased to 8 mL g⁻¹, the areal capacity decreased in the initial 20 cycles and showed lower areal capacity in the following cycling, which is ascribed to aggravated polarization derived from high viscosity of the electrolyte and poor ion transportation.^[27] Even so, the MoS₂–MoN/S cathode still kept high stable cycling behavior with capacity retention of 82.8% after 100 cycles.

To further testify to the cycling performances aiming at commercial standards, the MoS₂–MoN host with ultra-high loadings of 12.2 mg cm⁻² (sulfur content of 72.7%) and lean electrolyte usage down to 4.2 mL g⁻¹ are also shown in Figure 6b. When the E/S = 8.3 mL g⁻¹, the MoS₂–MoN/S cathode delivered a high initial areal capacities of 13.3 mAh cm⁻² (corresponding specific capacity of 1106.3 mAh g⁻¹) and maintained high areal capacities of 10.3 mAh cm⁻² (capacity retention of 77.4%) after 100 cycles. When the E/S ratio decreased to 6.3 mL g⁻¹, the average capacity decreased to some extent but still could maintain the stable cycling performance. It indicates that the MoS₂–MoN host shows great superiority in achieving good sulfur electrochemistry with low usage of electrolyte. However, when the E/S ratio decreased to 4.2 mL g⁻¹, the MoS₂–MoN/S cathode showed much lower initial areal capacities due to the insufficient wetting of the electrode surface, which increased gradually to ≈10.9 mAh cm⁻² until 78th cycle. The corresponding galvanostatic charge/discharge profiles (Figure 6c) also showed the large voltage gap with poor ion transportation and aggravated polarization.^[5] The long-term cycling with optimized usage of E/S = 6.3 mL g⁻¹ of cathode at 0.5C are shown in Figure 6d, which shows a 200 cycles stable cycling with retention of 5.2 mAh cm⁻². More importantly, among the recently reported high-loading free-standing Li–S batteries cathodes (Figure 6e; Table S3, Supporting Information), the gravimetric energy densities of MoS₂–MoN/S cathodes in Li–S battery achieves a competitive performance of 266.7 Wh kg⁻¹ at a system level (considering the total mass of the cathode, electrolyte, separator, and Li metal), further

verifying the superiority of this heterostructure MoS₂–MoN host for advanced Li–S energy systems.

3. Conclusions

We proposed a heterostructure MoS₂–MoN host grown with NCNT arrays as a 3D free-standing cathode. In this heterostructure, we observed moderate LiPS trapping ability and fast surface Li⁺ diffusion (by MoS₂) together with high electron conductivity and coupled electron transfer through redox reaction (by MoN) for LiPS conversion, which was simultaneously realized, enabling an efficient multifunctional trapping-diffusion-catalytic conversion of LiPSs. Through the respective merits of MoS₂ and MoN, the MoS₂–MoN host could form a synergetic enhancement effect to restrain the shuttling effect. On basis of these fascinating superiorities, the MoS₂–MoN/S cathode has great potential in enabling high energy density and long cycle life Li–S batteries for advanced energy storage application.

4. Experimental Section

Preparation of MoS₂ Host: First, carbon paper was pretreated by coating a thin Al₂O₃ layer by atomic layer deposition. Second, free-standing NCNT paper was prepared by a chemical vapor deposition (CVD) method, as reported previously.^[2] Third, MoS₂ nanosheets were vertically grown on the NCNT arrays by using a facile hydrothermal method. In a typical synthesis procedure, 0.75 mmol Na₂MoO₄ · 2H₂O was dissolved in 45 mL distilled water with continuous stirring for 20 min, followed by addition of 3.75 mmol CH₄N₂S. The solution together with the NCNT array paper was transferred into a 50 mL Teflon-lined autoclave and heated at 200 °C for 20 h. After the hydrothermal process, the MoS₂ host was washed with distilled water and dried at 80 °C for 12 h.

Preparation of MoS₂–MoN Heterostructure Host: The MoS₂–MoN heterostructure host was prepared by using a facile in situ nitridation method. In a typical synthesis procedure, a piece of MoS₂ host was put into a quartz tube of a CVD furnace. Then, the furnace was heated up to 800 °C with the heating rate of 5 °C per min under Ar₂. After the temperature reached 800 °C, the furnace was held at 800 °C under the mixing gas (Ar₂:NH₃ = 5:1) for 30 min. The pure MoN host was treated with a similar process under the mixing gas (Ar₂: NH₃ = 5:1) for 2 h.

Materials Characterizations: The morphologies were characterized using field-emission SEM (Hitachi S-4800) and high-resolution TEM (JEOL 2010 FEG). XPS (ESCALAB 250Xi) was used to analyze the elemental composition and valence state. XRD (Bruker D8 advanced) and Raman spectroscopy (HORIBA Scientific LabRAM) were used to analyze the structure, composition and chemical bonds of these samples. The nitrogen sorption isotherm was recorded on a gas sorptometer (Micromeritics 3Flex 3500). XANES spectra of S K-edge and Mo L-edge were measured on SXRMB and Mo K-edge were measured on HXMA at the Canadian Light Source (CLS) in Saskatoon, Canada.

Polysulfide Adsorption Observations: Li₂S₄, Li₂S₆, and Li₂S₈ solutions were prepared by mixing Li₂S and S with a molar ratio of 1:3, 1:5, and 1:7, respectively, into a 1:1 (v/v) DOL/DME mixture. Scrapping off from the free-standing hosts, 5 mg of MoS₂, MoN, or MoS₂–MoN composite powder was separately added into a solution of 5 mmol L⁻¹ Li₂S₄, Li₂S₆, or Li₂S₈.

Li₂S Nucleation Tests: Li₂S₈ electrolyte (0.20 mol L⁻¹) was prepared by mixing sulfur and Li₂S at a molar ratio of 7:1 in a 1:1 DOL/DME (v/v) solutions followed by vigorous mixing for 24 h. A consistent amount of 20 mL Li₂S₈ electrolyte was first distributed onto the cathode and then 25 mL LiTFSI (1.0 mol L⁻¹) without Li₂S₈ was dropped onto the lithium

anode. The batteries were galvanostatically discharged to 2.06 V under 0.112 mA and held potentiostatically at 2.05 V until the current was below 0.01 mA for nucleation and growth of Li₂S. Based on Faraday's law, the energy was measured to evaluate the nucleation/growth rate of Li₂S on various host surfaces.

Electrochemical Characterizations: Standard CR2032-type coin cells were assembled in an Ar-filled glove box with oxygen and moisture content below 1 ppm. 40 μL sulfur-containing solution (20 mg.mL⁻¹ sulfur in CS₂) were dropped and casted on the host. To control the loadings of sulfur in cathode, the same process was repeated. The regular sulfur loading is ≈1.2 mg cm⁻². Electrodes with high areal sulfur loadings of 6.4 and 12.2 mg cm⁻² were also prepared to test the cycling stability. To compare the electrochemical performances under the different amounts of electrolyte, 80, 120, and 160 μL electrolyte (1.0 M LiTFSI dissolved in mixed solvents of DOL and DME (v/v = 1:1) with 1 wt% of LiNO₃) were used to assemble the coin cells. Through a VMP3 electrochemical workstation, the CV curves were performed at a scan rate of 0.1 mV s⁻¹ and electrochemical impedance spectroscopy (EIS) was tested with a frequency range of 200 kHz to 0.1 Hz.

Calculation Details: The first principle calculation was performed by using the CASTEP DFT code^[28] of Accelrys Material Studio with the exchange-correlation functional of Perdew-Burke-Ernzerh^[29] based on generalized gradient approximation. For geometry optimization of Li₂S₄, Li₂S₆, and Li₂S₈ molecules, the maximum final force of the convergence tolerance was set as 0.01 eV Å⁻¹, and the total energy of the system was utilized as 5.0 × 10⁻⁶ eV atom⁻¹. The free surface of MoS₂ (100) and MoN (100) slab was separated by a 14 Å vacuum layer in the vertical direction to allow for the adsorption of the polysulfide molecule (Li₂S₄, Li₂S₆, and Li₂S₈). Adsorption of the polysulfide molecule on the surface of MoS₂ (100) and MoN (100) slab was set on only one side of the exposed surfaces, with the dipole moment corrected accordingly in the z direction. We used a Gamma k-point mesh for the sampling of the Brillouin zone, and a cut-off energy of 330 eV. The threshold for self-consistent-field density convergence was set to 5.0 × 10⁻⁷ eV atom⁻¹. For quantitatively measuring the interaction between the substrates (MoS₂ (100) and MoN (100)) and polysulfide molecule (Li₂S₄, Li₂S₆, and Li₂S₈), the interacted energy E_i between the polysulfide molecule and the substrate is defined as follow

$$E_i = E_{\text{sub}} + E_{\text{polysulfide}} - E_{\text{total}} \quad (1)$$

where E_{sub}, E_{polysulfide}, and E_{total} represent the total energies of the substrate, the polysulfide molecule, and the adsorption pair of the substrate and polysulfide molecule, respectively. The LST/QST method^[30] is applied for computing Li⁺ transition state by the implemented in the CASTEP code. The diffusion energy barrier is the energy difference between the total energies of transition state and the initial defective structure.

Supporting Information

Supporting Information is available from the Wiley Online Library or from the author.

Acknowledgements

This research was supported by the National Natural Science Foundation of China (Grant Nos. 51875330 and 51975342), the Natural Science Foundation of Shaanxi Province (Grant Nos. 2018JZ5003 and 2019JZ-24), the China Postdoctoral Science Foundation (Grant Nos. 2020M683408 and 2020M673603XB), the Natural Science and Engineering Research Council of Canada (NSERC), the Canada Research Chair Program (CRC), the Canada Foundation for Innovation (CFI), the Ontario Research Foundation (ORF), and the Western University. The authors acknowledge the National Supercomputing Center in Shenzhen for providing the computational resources and materials studio (version 7.0, DMol 3

module). The authors thank the support from Dr. Weijia Wang at the Northwestern Polytechnical University for first principle calculations. The authors also thank the technical support from the Canadian Centre of Electron Microscopy (CCEM) at McMaster University for the TEM characterizations.

Conflict of Interest

The authors declare no conflict of interest.

Keywords

heterostructures, lithium–sulfur batteries, MoN, MoS₂, synergistic effect

Received: October 20, 2020

Revised: December 3, 2020

Published online: February 11, 2021

- [1] a) X. Yang, J. Luo, X. Sun, *Chem. Soc. Rev.* **2020**, *49*, 2140; b) X. Yang, X. Li, K. Adair, H. Zhang, X. Sun, *Electrochem. Energy Rev.* **2018**, *1*, 239.
- [2] S. Z. Wang, H. Y. Chen, J. X. Liao, Q. Sun, F. P. Zhao, J. Luo, X. T. Lin, X. B. Niu, M. Q. Wu, R. Y. Li, X. L. Sun, *ACS Energy Lett.* **2019**, *4*, 755.
- [3] a) Y. Hu, W. Chen, T. Lei, Y. Jiao, J. Huang, A. Hu, C. Gong, C. Yan, X. Wang, J. Xiong, *Adv. Energy Mater.* **2020**, *10*, 2000082; b) J. He, A. Bhargav, H. Yaghoobnejad Asl, Y. Chen, A. Manthiram, *Adv. Energy Mater.* **2020**, *10*, 2001017; c) J. He, Y. Chen, A. Manthiram, *Adv. Energy Mater.* **2019**, *9*, 1900584.
- [4] S. H. Chung, A. Manthiram, *Adv. Mater.* **2019**, *31*, 1901125.
- [5] a) J. He, L. Luo, Y. Chen, A. Manthiram, *Adv. Mater.* **2017**, *29*, 1702707; b) S. Z. Wang, J. X. Liao, X. F. Yang, J. N. Liang, Q. Sun, J. W. Liang, F. P. Zhao, A. Koo, F. P. Kong, Y. Yao, X. J. Gao, M. Q. Wu, S. Z. Yang, R. Y. Li, X. L. Sun, *Nano Energy* **2019**, *57*, 230.
- [6] a) D. Tian, X. Song, M. Wang, X. Wu, Y. Qiu, B. Guan, X. Xu, L. Fan, N. Zhang, K. Sun, *Adv. Energy Mater.* **2019**, *9*, 1901940; b) X. J. Gao, X. F. Yang, M. S. Li, Q. Sun, J. N. Liang, J. Luo, J. W. Wang, W. H. Li, J. W. Liang, Y. L. Liu, S. Z. Wang, Y. F. Hu, Q. F. Xiao, R. Y. Li, T. K. Sham, X. L. Sun, *Adv. Funct. Mater.* **2019**, *29*, 1806724.
- [7] X. Yang, X. Gao, Q. Sun, S. P. Jand, Y. Yu, Y. Zhao, X. Li, K. Adair, L. Y. Kuo, J. Rohrer, J. Liang, X. Lin, M. N. Banis, Y. Hu, H. Zhang, X. Li, R. Li, H. Zhang, P. Kaghazchi, T. K. Sham, X. Sun, *Adv. Mater.* **2019**, *31*, 1901220.
- [8] F. Y. Fan, M. S. Pan, K. C. Lau, R. S. Assary, W. H. Woodford, L. A. Curtiss, W. C. Carter, Y.-M. Chiang, *J. Electrochem. Soc.* **2016**, *163*, A3111.
- [9] a) B. Zhang, C. Luo, Y. Deng, Z. Huang, G. Zhou, W. Lv, Y. B. He, Y. Wan, F. Kang, Q. H. Yang, *Adv. Energy Mater.* **2020**, *10*, 2000091; b) R. Fang, S. Zhao, Z. Sun, D.-W. Wang, R. Amal, S. Wang, H.-M. Cheng, F. Li, *Energy Storage Mater.* **2018**, *10*, 56.
- [10] T. Zhou, W. Lv, J. Li, G. Zhou, Y. Zhao, S. Fan, B. Liu, B. Li, F. Kang, Q.-H. Yang, *Energy Environ. Sci.* **2017**, *10*, 1694.
- [11] Y. Song, W. Zhao, L. Kong, L. Zhang, X. Zhu, Y. Shao, F. Ding, Q. Zhang, J. Sun, Z. Liu, *Energy Environ. Sci.* **2018**, *11*, 2620.
- [12] a) J. He, G. Hartmann, M. Lee, G. S. Hwang, Y. Chen, A. Manthiram, *Energy Environ. Sci.* **2019**, *12*, 344; b) B. Yu, Y. Chen, Z. Wang, D. Chen, X. Wang, W. Zhang, J. He, W. He, *J. Power Sources* **2020**, *447*, 227364; c) Y. Pan, L. Gong, X. Cheng, Y. Zhou, Y. Fu, J. Feng, H. Ahmed, H. Zhang, *ACS Nano* **2020**, *14*, 5917.
- [13] A. Habib, F. Florio, R. Sundararaman, *J. Opt.* **2018**, *20*, 064001.

- [14] R. Li, X. Zhou, H. Shen, M. Yang, C. Li, *ACS Nano* **2019**, *13*, 10049.
- [15] Z. A. Ghazi, X. He, A. M. Khattak, N. A. Khan, B. Liang, A. Iqbal, J. Wang, H. Sin, L. Li, Z. Tang, *Adv. Mater.* **2017**, *29*, 1606817.
- [16] R. Li, H. Peng, Q. Wu, X. Zhou, J. He, H. Shen, M. Yang, C. Li, *Angew. Chem., Int. Ed. Engl.* **2020**, *59*, 12129.
- [17] a) A. Eckmann, A. Felten, A. Mishchenko, L. Britnell, R. Krupke, K. S. Novoselov, C. Casiraghi, *Nano Lett.* **2012**, *12*, 3925; b) X. Geng, W. Sun, W. Wu, B. Chen, A. Al-Hilo, M. Benamara, H. Zhu, F. Watanabe, J. Cui, T. P. Chen, *Nat. Commun.* **2016**, *7*, 10672.
- [18] J. Zhou, X. Liu, L. Zhu, J. Zhou, Y. Guan, L. Chen, S. Niu, J. Cai, D. Sun, Y. Zhu, J. Du, G. Wang, Y. Qian, *Joule* **2018**, *2*, 2681.
- [19] G. Zhou, H. Tian, Y. Jin, X. Tao, B. Liu, R. Zhang, Z. W. Seh, D. Zhuo, Y. Liu, J. Sun, J. Zhao, C. Zu, D. S. Wu, Q. Zhang, Y. Cui, *Proc. Natl. Acad. Sci. USA* **2017**, *114*, 840.
- [20] H.-J. Peng, G. Zhang, X. Chen, Z.-W. Zhang, W.-T. Xu, J.-Q. Huang, Q. Zhang, *Angew. Chem., Int. Ed.* **2016**, *55*, 12990.
- [21] Y. N. Zhou, J. Ma, E. Hu, X. Yu, L. Gu, K. W. Nam, L. Chen, Z. Wang, X. Q. Yang, *Nat. Commun.* **2014**, *5*, 5381.
- [22] C. Ye, Y. Jiao, H. Jin, A. D. Slattery, K. Davey, H. Wang, S. Z. Qiao, *Angew. Chem., Int. Ed.* **2018**, *57*, 16703.
- [23] X. Li, A. Lushington, Q. Sun, W. Xiao, J. Liu, B. Wang, Y. Ye, K. Nie, Y. Hu, Q. Xiao, R. Li, J. Guo, T. K. Sham, X. Sun, *Nano Lett.* **2016**, *16*, 3545.
- [24] M. Wang, L. Fan, D. Tian, X. Wu, Y. Qiu, C. Zhao, B. Guan, Y. Wang, N. Zhang, K. Sun, *ACS Energy Lett.* **2018**, *3*, 1627.
- [25] a) S. Z. Wang, F. Gong, S. Z. Yang, J. X. Liao, M. Q. Wu, Z. Q. Xu, C. Chen, X. F. Yang, F. P. Zhao, B. Wang, Y. S. Wang, X. L. Sun, *Adv. Funct. Mater.* **2018**, *28*, 1801806; b) Y. Song, J. Liao, C. Chen, J. Yang, J. Chen, F. Gong, S. Wang, Z. Xu, M. Wu, *Carbon* **2019**, *142*, 697.
- [26] H. L. Pan, K. S. Han, M. H. Engelhard, R. G. Cao, J. Z. Chen, J. G. Zhang, K. T. Mueller, Y. Y. Shao, J. Liu, *Adv. Funct. Mater.* **2018**, *28*, 1707234.
- [27] W. Xue, Z. Shi, L. Suo, C. Wang, Z. Wang, H. Wang, K. P. So, A. Maurano, D. Yu, Y. Chen, L. Qie, Z. Zhu, G. Xu, J. Kong, J. Li, *Nat. Energy* **2019**, *4*, 374.
- [28] S. J. Clark, M. D. Segall, C. J. Pickard, P. Hasnip, M. I. J. Probert, K. Refson, M. C. Payne, *Zeitschrift Fur Kristallographie* **2005**, *220*, 567.
- [29] J. P. Perdew, K. Burke, M. Ernzerhof, *Phys. Rev. Lett.* **1996**, *77*, 3865.
- [30] N. Govind, M. Petersen, G. Fitzgerald, D. King-Smith, J. Andzelm, *Comput. Mater. Sci.* **2003**, *28*, 250.